RSC Advances

PAPER

View Article Online
View Journal | View Issue

Cite this: *RSC Adv.*, 2026, **16**, 11117

Comprehensive analysis of $Rb_2Mg_2(WO_4)_3$: structural, morphological, dielectric, and CBH model-based charge transport for optoelectronic applications

Ines Mbarek,[a] Saber Nasri,[a] Iheb Garoui,[a] Mehdi Akermi,[b] Mohamed Tliha[c] and Abderrazek Oueslati *[a]

In this study, a novel $Rb_2Mg_2(WO_4)_3$ triple tungstate was successfully synthesized *via* a conventional solid-state reaction and comprehensively characterized for its structural, microstructural, and dielectric properties—key attributes for next-generation microelectronic applications. High-resolution X-ray diffraction confirmed a rare single-phase cubic structure (space group $P2_13$), a significant finding given the structural complexity of mixed-cation tungstates. Scanning electron microscopy coupled with energy-dispersive X-ray spectroscopy revealed a highly uniform microstructure with an average grain size of 8.16 μm and stoichiometric elemental composition, ensuring reliable bulk properties. Impedance spectroscopy provided critical insights, displaying Nyquist plots with two distinct depressed semicircles that delineate grain and grain-boundary contributions, hallmarking non-Debye relaxation behavior. These were precisely modeled using the equivalent circuit $(R_1\|CPE_1)$ + $(R_2\|CPE_2)$, unveiling thermally activated charge transport: resistances decreased with rising temperature, accompanied by intensified interfacial polarization. A synergistic impedance-modulus analysis revealed a pivotal transition from localized to long-range conduction, a cornerstone for understanding ion dynamics in such materials. AC conductivity and dielectric loss data, rigorously analyzed through the correlated barrier hopping (CBH) model, unequivocally confirmed a hopping-dominated transport mechanism—offering new mechanistic depth to tungstate-based dielectrics. Notably, $Rb_2Mg_2(WO_4)_3$ exhibits exceptionally high permittivity alongside ultra-low dielectric loss, positioning it as a standout candidate for high-performance capacitors, microwave devices, and advanced microelectronics. This work not only advances the fundamental understanding of charge transport in complex tungstates but also paves the way for their practical deployment in energy-efficient technologies.

Received 20th December 2025
Accepted 18th February 2026

DOI: 10.1039/d5ra09859a

rsc.li/rsc-advances

Introduction

Tungstate materials have recently attracted significant research attention due to their outstanding applications across various fields of science and technology.[1–3] Furthermore, certain tungstates are gaining interest as materials for laser hosts[4] and energy storage.[5,6] These outstanding properties of tungstates arise from the ability of tungsten to flexibly adopt both WO_4 and WO_6 coordination geometries, which can connect with other polyhedra to create various framework structures. For example, in compounds with the chemical formula $A_4Mg(WO_4)_3$ (A = Na, K), $Na_4Mg(WO_4)_3$ (ref. 7) crystallizes in the monoclinic space group $C2/c$, while $K_4Mg(WO_4)_3$, possessing an identical stoichiometry to $Na_4Mg(WO_4)_3$, exhibits a different framework structure with triclinic symmetry and the space group $P\bar{1}$. Other tungstate compounds with diverse structures include $BaWO_4$ (ref. 8) (scheelite, tetragonal), $NiWO_4$ (ref. 9) (wolframite, monoclinic), and Bi_2WO_6 (ref. 10) (perovskite-layered, orthorhombic), each exhibiting distinct atomic arrangements and coordination environments. Lead tungstate ($PbWO_4$)[11] also crystallizes in the tetragonal scheelite structure, while uranyl tungstates like $M_2(UO_2)(W_2O_8)$ (M = Na, K)[12] form layered structures with WO_4 tetrahedra, WO_5 square pyramids, and WO_6 octahedra, leading to varied frameworks. Our group studies $Na_4Mg(WO_4)_3$ (ref. 7) and $Li_2Mg_2(WO_4)_3$,[13] both showing high dielectric constants (~10^5), low dielectric losses, and semiconducting behavior. $Na_4Mg(WO_4)_3$ has a monoclinic structure with thermally activated charge transport, while $Li_2Mg_2(WO_4)_3$ is orthorhombic with long-range charge mobility.

[a]*Laboratory of Spectroscopic and Optical Characterization of Materials (LaSCOM), Faculty of Sciences, University of Sfax, B. P. 1171, 3000 Sfax, Tunisia. E-mail: oueslatiabderrazek@yahoo.fr*

[b]*Department of Physics Sciences, College of Science, Jazan University, P.O. Box. 114, Jazan 45142, Kingdom of Saudi Arabia. E-mail: makermi@jazanu.edu.sa*

[c]*Department of Physics, Al-Qunfudah University College, Umm Al-Qura University, Saudi Arabia*

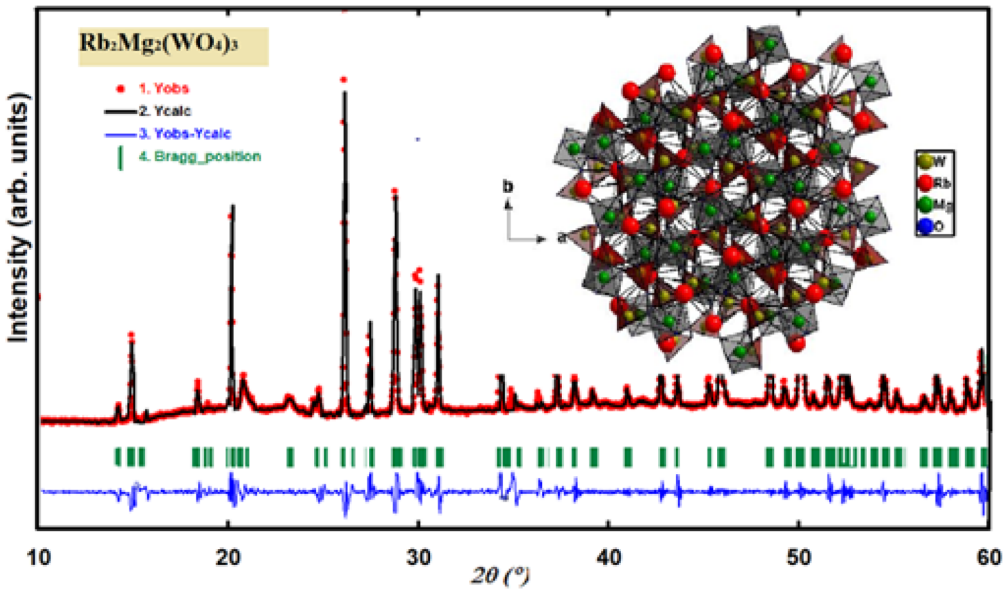

Fig. 1 The Rietveld refinement XRD of the synthesized $Rb_2Mg_2(WO_4)_3$ at room temperature. Inset: projection of the crystal structure of $Rb_2Mg_2(WO_4)_3$ into (001) plane.

Both materials exhibit promising electrical properties for optoelectronic and energy storage applications. Inspired by continuing the above idea, we mainly focus on $Rb_2Mg_2(WO_4)_3$, which has been rarely studied.[14] Let us return to the history of this material; $Rb_2Mg_2(WO_4)_3$, was first studied in 2015.[14] Since $Rb_2Mg_2(WO_4)_3$ crystallizes in a cubic system, its atomic arrangement is consistent along the *a*-, *b*-, and *c*-axis. Inset Fig. 1 illustrates the atomic arrangement along the *c*-axis, showing that the structure forms a three-dimensional framework made up of isolated WO_4 tetrahedra, MgO_6 octahedra, and RbO_{12} polyhedra.[14]

The selection of $Rb_2Mg_2(WO_4)_3$ is part of a systematic study on how A-site cation substitution affects the dielectric properties of langbeinite-type tungstates. Compared to smaller alkali ions like Na^+ or K^+, the larger Rb^+ ion increases lattice rigidity and reduces free volume within the structure, enhancing thermal stability and suppressing leakage currents at high temperatures. This makes $Rb_2Mg_2(WO_4)_3$ a promising candidate for high-temperature insulation applications, offering advantages over lighter alkali-metal analogs.[14] Building on these findings, the present study focuses on $Rb_2Mg_2(WO_4)_3$, a relatively unexplored cubic tungstate. Its structural and dielectric properties were investigated to assess its potential for applications in optoelectronics and energy storage. Furthermore, the conduction mechanism was elucidated through complementary electrical analyses.

Experimental details

In this study, the $Rb_2Mg_2(WO_4)_3$ compound was synthesized *via* a solid-state reaction method using high-purity WO_3, Rb_2CO_3, and MgO as starting materials. The raw materials were combined in a molar ratio of $WO_3 : Rb_2CO_3 : MgO = 3 : 1 : 2$ and then pressed into pellets. To counteract lithium loss caused by volatilization, an additional 2 mol% of Rb_2CO_3 was incorporated. The mixture underwent solid-state sintering at 900 °C for 120 hours in air, resulting in the formation of the $Rb_2Mg_2(WO_4)_3$ phase.

The crystal structure of the synthesized samples was characterized using a Philips X'Pert X-ray powder diffractometer with Cu-Kα radiation (λ = 1.5418 Å). Diffraction data were collected across a Bragg angle range of 10° to 60° with a step size of 0.05°, and structural refinement was performed by Rietveld analysis[15] using the FULLPROF software.[16]

Morphology and particle size were examined through scanning electron microscopy (SEM), while elemental composition was confirmed by energy-dispersive X-ray spectroscopy (EDX).

For electrical characterization, the powder was pressed into tablets measuring 8 mm in diameter and 1 mm in thickness under a uniaxial pressure of 3 t cm^{-2}. Silver conductive layers were applied to both surfaces to serve as electrodes in an Ag/electrolyte/Ag configuration. Impedance measurements were carried out using a Solartron 1260 Impedance Analyzer over a frequency range from 0.1 Hz to 5 MHz, controlled by a microcomputer, within a temperature range of 473 to 673 K, which was selected to focus on the high-temperature cubic phase, where ionic conductivity is most prominent. Below 473 K, the material's properties remain nearly constant, exhibiting negligible variation that does not contribute significantly to the phenomenon under study. Above 673 K, the study was limited to ensure the chemical stability of the tungstate framework and to avoid potential sample–electrode interactions. However, the cubic structure is expected to remain stable until it approaches its melting point.

Results and discussion

Structural study

The X-ray diffraction (XRD) pattern of $Rb_2Mg_2(WO_4)_3$, shown in Fig. 1, indicates the formation of a pure single-phase

Table 1 Rietveld refined parameters for $Rb_2Mg_2(WO_4)_3$ compound

$Rb_2Mg_2(WO_4)_3$ compound at room temperature	
System	Cubic
Space group	$P2_13$
$a = b = c$	10.7584 (6)
=	90
=	90
Γ	90
Volume (Å^3)	1244.15 (12)
χ^2	2.04
Crystallite size	72 nm

compound. All observed peaks are consistent with a cubic crystal structure belonging to the $P2_13$ space group.

The structure was further analyzed and refined using the Rietveld method, with the refinement results summarized in Table 1, based on its lattice parameters and space group, the crystal structure of $Rb_2Mg_2(WO_4)_3$ is consistent with previously reported structures in the literature.[14]

X-ray diffraction (XRD) analysis is employed to estimate the crystallite size of the material. The average crystallite size D is determined using the Debye–Scherrer equation:[17]

$$D = \frac{K\lambda}{\beta_D \cos(\theta)} \quad (1)$$

In this context, K is the shape factor, taken as 0.9, and λ corresponds to the wavelength of Cu Kα radiation. The parameter β represents the full width at half maximum (FWHM) of the most intense diffraction peak among all observed reflections, while θ is the Bragg diffraction angle. The FWHM β characterizes the broadening of the diffraction peaks, which arises from the finite crystallite size and the presence of microstrain within the material. The calculated crystallite size D is summarized in Table 1. The calculated crystallite size is 72 nm. It is important to distinguish this from the grain size observed in later SEM analysis; the crystallite size provides a more statistically meaningful measure of the bulk material's structural integrity, whereas SEM highlights the surface-sensitive grain agglomeration. In tungstate compounds, crystallite dimensions in the nanometer scale are known to significantly influence electrical behavior, frequently resulting in enhanced conductivity and improved catalytic activity. These improvements are commonly attributed to the larger specific surface area and the emergence of size-dependent (quantum) effects in nanostructured systems. Consequently, a detailed and systematic electrical characterization was undertaken.

Morphology analysis

The microstructural features of $Rb_2Mg_2(WO_4)_3$ were investigated using scanning electron microscopy (SEM). As illustrated in Fig. 2, the SEM images reveal grains that are relatively uniform in size and well-distributed at the micrometer scale. At low magnification (100×), the surface appears smooth and continuous, with no visible cracks or significant voids, indicating that the synthesis process produced a high-quality material.

At higher magnifications (up to 6403×), a more detailed granular texture is observed, consisting of compact aggregates and distinct particles. The clearly defined particle boundaries and heterogeneous arrangement suggest a polycrystalline microstructure. The surface morphology and grain size distribution of the $Rb_2Mg_2(WO_4)_3$ compound were investigated *via*

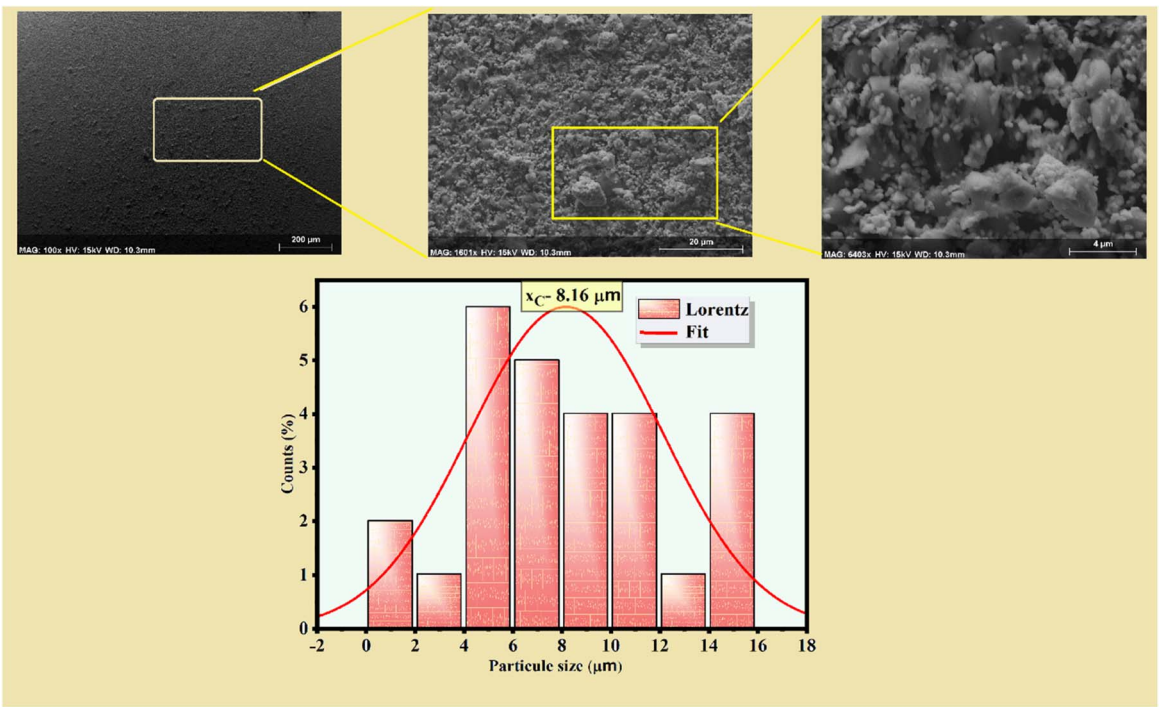

Fig. 2 (a) Scanning electron microscopy images, (b) distribution histogram of grains.

SEM, as illustrated in Fig. 2. The micrographs reveal an irregular, polygonal morphology with a tendency toward agglomeration, typical of materials processed through high-temperature solid-state reaction. Due to the non-spherical nature of the grains, a statistical analysis was performed by measuring the Feret diameter of a significant number of particles using imageJ analysis software.[18] The resulting histogram (Fig. 2) represents the particle size distribution, which was successfully fitted using a Lorentzian function. This fitting yields a mean particle size of approximately 8.16 μm.

The densely packed, interconnected grains are expected to positively influence properties such as optical clarity, electrical transport, and mechanical stability, underscoring the potential of $Rb_2Mg_2(WO_4)_3$ for advanced materials applications. To assess the qualitative composition and purity of the synthesized material, energy-dispersive X-ray microanalysis (EDX) was performed. The EDX spectrum, along with quantitative analysis, as shown in Fig. 3, confirms the presence of oxygen, magnesium, rubidium, and tungsten as the primary elements. According to the weight percent chart, tungsten is the most abundant element (54.94%), followed by oxygen (19.63%), rubidium (21.63%), and magnesium (3.78%). The atomic percent distribution differs, with oxygen dominating at 63.55%, and a notable presence of tungsten (15.26%), rubidium (13.13%), and magnesium (8.06%). These results suggest successful synthesis and homogeneity at the compositional level, with the expected stoichiometry consistent with the compound's nominal formula. The high oxygen and tungsten content, corroborated by the intense peaks in the spectrum, are indicative of the WO_4 units, while rubidium and magnesium peaks confirm their role in the lattice structure. The observed atomic ratio ($Rb:Mg:W:O = 1.63:1:1.89:7.88$) shows a deviation from the theoretical 2 : 2 : 3 : 12 stoichiometry. This variance is primarily associated with the semi-quantitative nature of the EDX technique,[19] particularly the lower sensitivity and high absorption corrections required for light elements like Oxygen.[20] Furthermore, a slight deficiency in Rubidium may be attributed to the partial volatilization of alkali cations during the high-temperature calcination process required for langbeinite formation.[21] These deviations likely result from rubidium volatilization, intrinsic defects, and EDX's surface sensitivity.[22] Despite these deviations, the consistent presence of all precursor elements and the absence of secondary phases in the XRD patterns confirm the successful formation of the $Rb_2Mg_2(WO_4)_3$ phase.

Electrical properties

The electrical behavior of $Rb_2Mg_2(WO_4)_3$ was investigated using complex impedance spectroscopy over a temperature range of 473–673 K to elucidate its conduction mechanisms. To improve clarity, the Nyquist data were presented in two separate plots: Fig. 4(a) for 473–573 K and Fig. 4(b) for 593–673 K, as variations across the full temperature range were not clearly visible on a single figure.

The Nyquist plots exhibit two distinct semicircles corresponding to the contributions from grains at high frequencies and grain boundaries at low frequencies. In all spectra, the centers of the arcs lie below the Z′ axis, indicating non-Debye relaxation behavior.[23] The relative prominence of the two arcs varies with temperature: at lower temperatures, the grain-boundary response dominates, whereas at higher temperatures, the grain contribution becomes increasingly significant.

To rationalize these features, an equivalent circuit incorporating separate grain and grain-boundary contributions, each modeled by a resistance (R_g, R_{gb}) in parallel with a constant phase element (CPE_1, CPE_2) was applied, as shown in the insert of Fig. 4(a). At low temperatures, the large semicircles correspond to higher resistive behavior, while at higher temperatures, the reduction in arc size and the shift in impedance characteristics point to thermally activated charge transport. The close overlap between the red fitted curves and the experimental data confirms the suitability of the proposed circuit

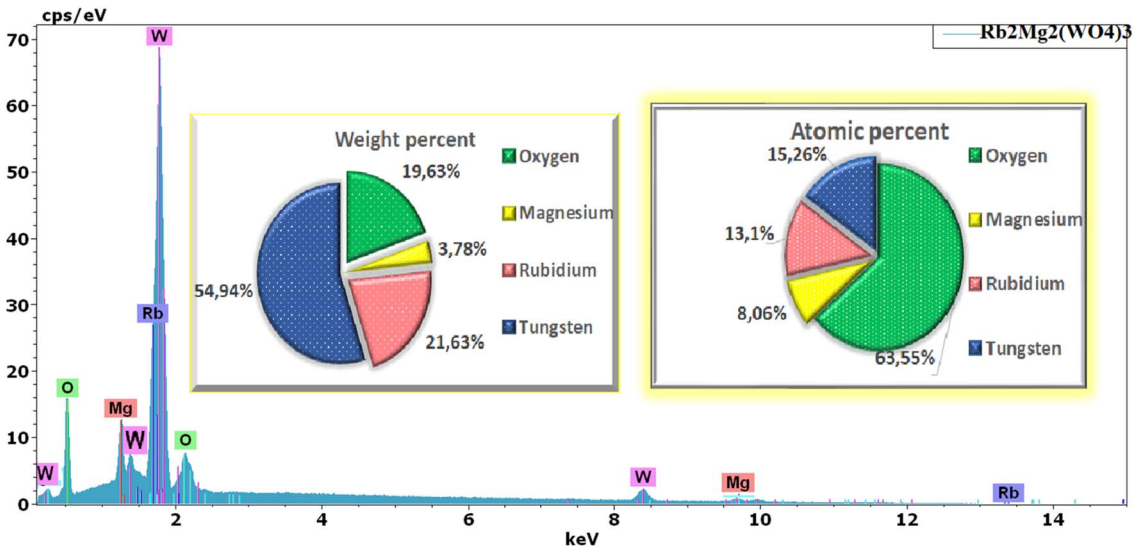

Fig. 3 EDX spectrum of the compound $Rb_2Mg_2(WO_4)_3$.

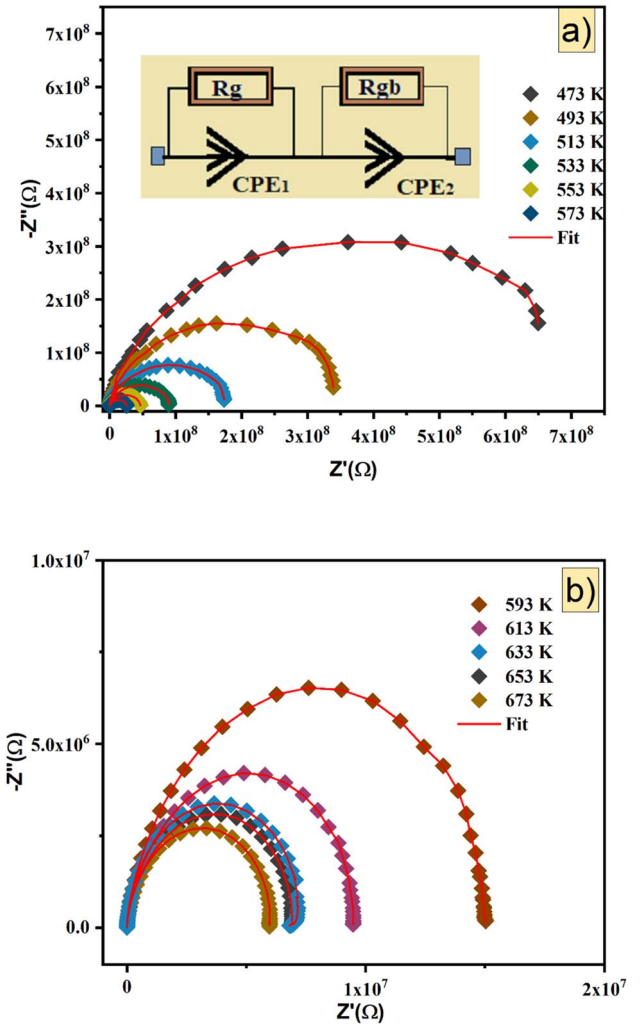

Fig. 4 (a) Nyquist plot of $Rb_2Mg_2(WO_4)_3$ compound, from 473 to 573 K. (b): Nyquist plot of $Rb_2Mg_2(WO_4)_3$ compound, from 493 to 673 K.

model and underscores the distinct electrical responses of the grain interiors and boundaries in $Rb_2Mg_2(WO_4)_3$. The impedance of the fractal interface capacitance, represented by the constant phase element (CPE), is calculated using the expression[24]

$$Z_{\mathrm{CPE}} = \frac{1}{Q(j\omega)^{\alpha}} \tag{2}$$

In this expression, Q denotes the capacitance value, and the parameter α indicates the extent of deviation of the semicircle from an ideal shape. Specifically, $\alpha = 1$ corresponds to ideal capacitive behavior, whereas $\alpha = 0$ corresponds to purely resistive behavior.

To accurately reproduce the frequency-dependent impedance behavior, the real (Z') and imaginary ($-Z''$) components were fitted using analytical expressions derived from the chosen model. These expressions explicitly incorporate the frequency dependence of the constant phase elements (CPEs) and are formulated as follows:

$$Z' = \frac{R_1\left(1 + R_1Q_1\omega^{\alpha_1}\cos\left(\alpha_1\frac{\pi}{2}\right)\right)}{\left[1 + R_1Q_1\omega^{\alpha_1}\cos\left(\alpha_1\frac{\pi}{2}\right)\right]^2 + \left[1 + R_1Q_1\omega^{\alpha_1}\sin\left(\alpha_1\frac{\pi}{2}\right)\right]^2} + \frac{R_2\left(1 + R_2Q_2\omega^{\alpha_2}\cos\left(\alpha_2\frac{\pi}{2}\right)\right)}{\left[1 + R_2Q_2\omega^{\alpha_2}\cos\left(\alpha_2\frac{\pi}{2}\right)\right]^2 + \left[1 + R_2Q_2\omega^{\alpha_1}\sin\left(\alpha_2\frac{\pi}{2}\right)\right]^2} \tag{3}$$

$$-Z'' = \frac{{R_1}^2Q_1\omega^{\alpha_1}\sin\left(\alpha_1\frac{\pi}{2}\right)}{\left[1 + R_1Q_1\omega^{\alpha_1}\cos\left(\alpha_1\frac{\pi}{2}\right)\right]^2 + \left[1 + R_1Q_1\omega^{\alpha_1}\sin\left(\alpha_1\frac{\pi}{2}\right)\right]^2} + \frac{{R_2}^2Q_2\omega^{\alpha_2}\sin\left(\alpha_2\frac{\pi}{2}\right)}{\left[1 + R_2Q_2\omega^{\alpha_1}\cos\left(\alpha_2\frac{\pi}{2}\right)\right]^2 + \left[1 + R_2Q_2\omega^{\alpha_2}\sin\left(\alpha_2\frac{\pi}{2}\right)\right]^2} \tag{4}$$

The frequency-dependent behavior of the real part of the impedance (Z') for the investigated sample across a wide temperature range, as shown in the Fig. 5(a) and (b). Z′ is high at low frequencies, especially at lower temperatures, indicating the dominant role of grain boundary resistance and possible space charge accumulation. As frequency increases, Z′ decreases due to reduced interfacial polarization and the increasing contribution of grain conduction, with the minimum value at high frequencies decreasing as temperature rises, suggesting thermally activated conductivity.

Meanwhile, Fig. 6(a) and 6b showcase the imaginary part of the impedance ($-Z''$) as a function of angular frequency (ω) for a material studied across a broad temperature range. Panel (a) details the response from 473 K to 573 K, while panel (b) covers higher temperatures between 593 K and 673 K, showing a clear relaxation peak at each temperature. This peak shifts to higher frequencies and diminishes in magnitude with rising temperature, reflecting a thermally activated relaxation process with shorter relaxation times at elevated temperatures. The lack of multiple peaks points to a single dominant relaxation mechanism, likely associated with grain boundaries, while the asymmetric and broadened peak shape indicates non-Debye relaxation, consistent with the use of constant phase elements in the equivalent circuit model. Overall, these results confirm the semiconducting nature of the material and efficient conduction across grains and grain boundaries at higher temperatures. A quantitative assessment of these findings was carried out by examining the temperature dependence of the extracted resistance and capacitance values.

The corresponding bar charts are displayed in Fig. 7. As shown in Fig. 7(a), both the grain resistance (R_1) and grain-boundary resistance (R_2) undergo a pronounced decline as temperature rises, a trend typical of semiconducting systems in which thermal activation promotes charge-carrier mobility.[25] Conversely, the capacitance parameters associated with the constant-phase elements (Q_1 and Q_2), illustrated in Fig. 7(b) and (c), increase markedly with temperature. This enhancement is consistent with strengthened dielectric polarization and the

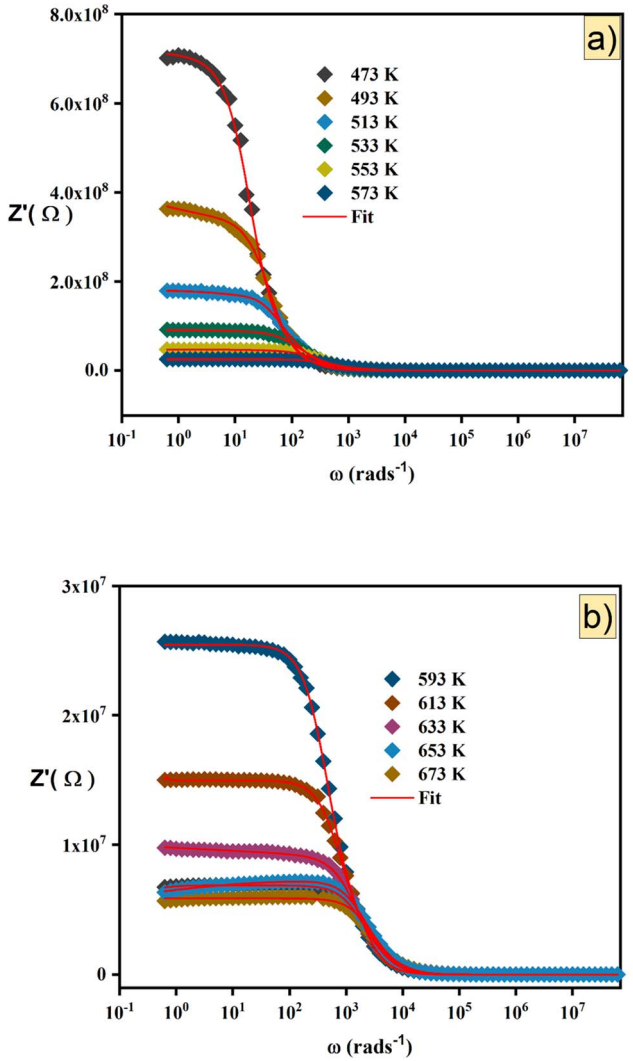

Fig. 5 (a) Frequency dependence of Z′ at different temperatures (from 473 to 573 K). (b): Frequency dependence of Z′ at different temperatures (from 493 to 673 K).

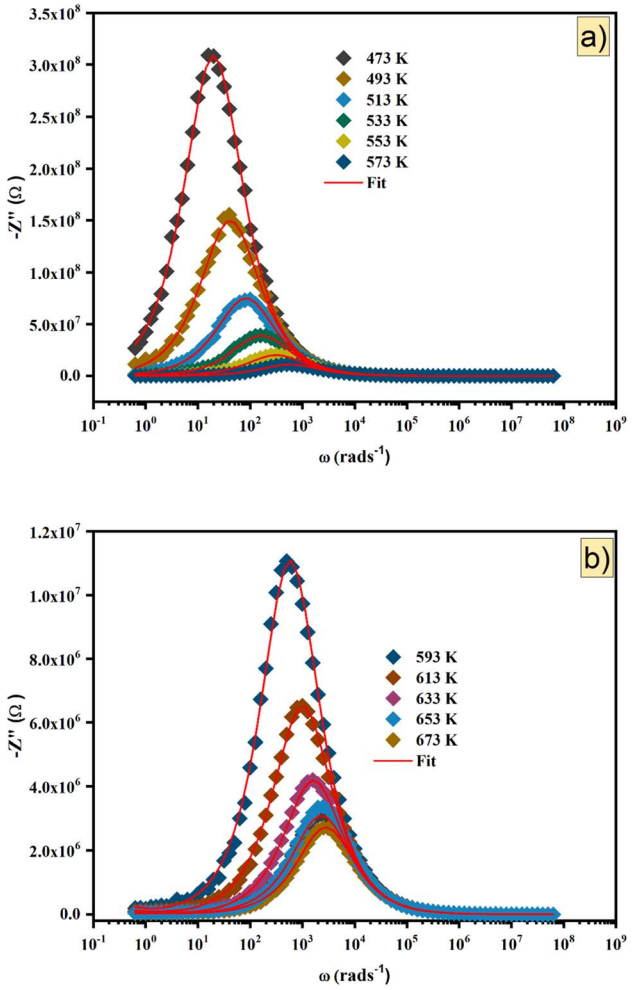

Fig. 6 (a) Frequency dependence of Z″ at different temperatures (from 473 to 573 K). (b): Frequency dependence of Z″ at different temperatures (from 493 to 673 K).

growing contribution of thermally activated dipolar or space-charge processes. Taken together, these trends reveal more efficient charge-storage behavior and intensified interfacial polarization at higher temperatures, underscoring the effective thermal activation of both conduction and point to the existence of relatively weak interfacial barriers, consistent with the behavior inferred from the Nyquist response.[26]

Modulus analysis

A detailed analysis of the dielectric modulus provides a valuable approach for investigating charge-transport processes in ceramic materials and for elucidating the microscopic mechanisms underlying dielectric relaxation.[27]

The complex dielectric modulus, M^*, is formally introduced as the inverse of the complex permittivity, ε^*

$$M^* = \frac{1}{\varepsilon^*} = j\omega C_0 Z^* = M' + jM'' \quad (5)$$

Here, M′ and M″ denote the real and imaginary components of the dielectric modulus, respectively, $C_0 = \frac{\varepsilon_0 A}{d}$ is the geometric capacitance (where ε_0 = vacuum permittivity, A = surface, d = thickness).

The real and imaginary components of the complex modulus can be written as

$$M' = \frac{\varepsilon'}{\varepsilon'^2 + \varepsilon''^2} \quad (6)$$

$$M'' = \frac{\varepsilon''}{\varepsilon'^2 + \varepsilon''^2} \quad (7)$$

Here, ε' and ε'' denote the real and imaginary components of the dielectric permittivity, respectively. Fig. 8(a) presents the frequency-dependent evolution of the real modulus (M') at various temperatures. At low frequencies, M' remains close to zero, indicating minimal restoring force for the electric field. With increasing frequency, M' progressively rises and eventually reaches a temperature-dependent saturation value. This

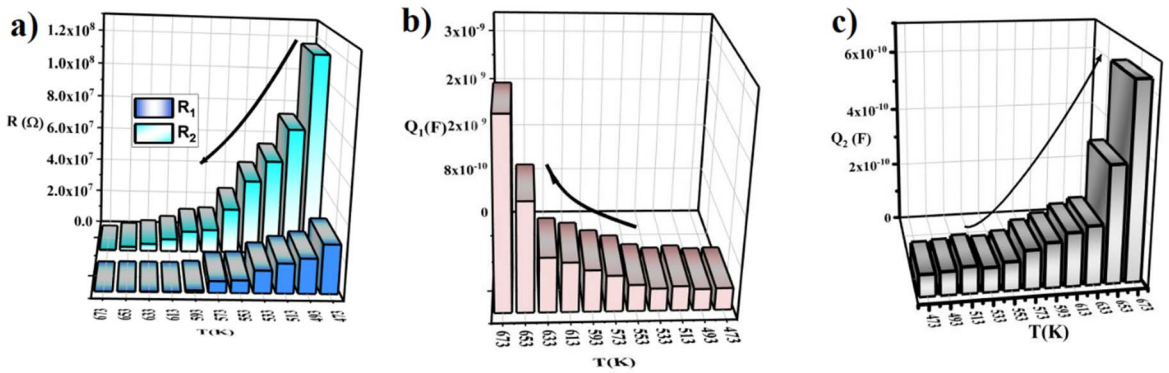

Fig. 7 Temperature dependence of the resistance and constant phase element (CPE) parameters extracted from Nyquist plot fittings: (a) grain resistance R_1, grain boundary resistance R_2, (b) grain CPE capacitance Q_1, and (c) grain boundary CPE capacitance Q_2.

saturation frequency shifts with temperature, and the magnitude of the saturated M' increases as the temperature rises. Such behavior is typically linked to the underlying conduction mechanism, where the mobility of thermally activated charge carriers governs the modulus response. As the temperature increases, the enhanced mobility of these carriers leads to a higher saturation level of M'. The observed decrease in the real component of the complex modulus M′ at frequencies exceeding 10^6 rads^{-1} is primarily attributed to the dielectric relaxation of the Rb^+ cation hopping mechanism within the langbeinite-type framework. As the frequency increases, the heavy rubidium ions, situated in relatively large interstitial sites, fail to maintain phase with the rapidly oscillating electric field, leading to a "freezing out" of their contribution to the material's total polarizability.[28] This transition from a long-range hopping regime to a localized vibrational regime results in a characteristic dispersion in the modulus formalism, a phenomenon well-documented in langbeinite-type structures where alkali metal dynamics dominate the radio-frequency response.[29] Furthermore, the complex network of corner-sharing WO_4 tetrahedra reaches its limit of electronic and atomic polarizability in this range, where the onset of WO_4 vibrational modes may contribute to the downturn of the storage component.[30] In polycrystalline samples, this behavior is further intensified by the Maxwell–Wagner–Sillars (MWS) effect, where the accumulation of charges at grain boundaries becomes negligible as the period of the applied field becomes shorter than the relaxation time of the boundary-trapped charges.

Nevertheless, rising temperatures increase the mobility of charge carriers, which in turn raises the overall saturation level of M'. At a given temperature, the maximum of M'' coincides with the minimum-tangent point of M', in good agreement with Bergman's empirical model. In this framework, the relaxation frequency associated with the M' peak marks the crossover from long-range to short-range ionic motion as the probing frequency increases.

Fig. 8(b) presents the frequency dependence of the imaginary modulus M'', revealing three characteristic regions. In the low-frequency domain situated below the M'' peak maximum M'' $(2\pi f_{\max}^{M''}\tau_{M''} < 1)$, charge carriers possess sufficient time to undertake long-range movements, enabling ions to hop between adjacent sites (long-distance hopping).[31] In contrast, at high frequencies beyond the M'' peak $(2\pi f_{\max}^{M''}\tau_{M''} > 1)$, most carriers become confined within their local potential wells, exhibiting only localized, short-range motion.[7] At the peak position $(2\pi f_{\max}^{M''}\tau_{M''} = 1)$, the system undergoes the transition between these two regimes.

The M'' response was modeled using the modified Kohlrausch–Williams–Watts (KWW) function proposed by Bergman:[32]

$$M'' = \frac{M''_{\max}}{(1-\beta) + \frac{\beta}{(1+\beta)}\left[\beta\left(\frac{\omega_{\max}}{\omega}\right) + \left(\frac{\omega}{\omega_{\max}}\right)^{\beta}\right]} \quad (8)$$

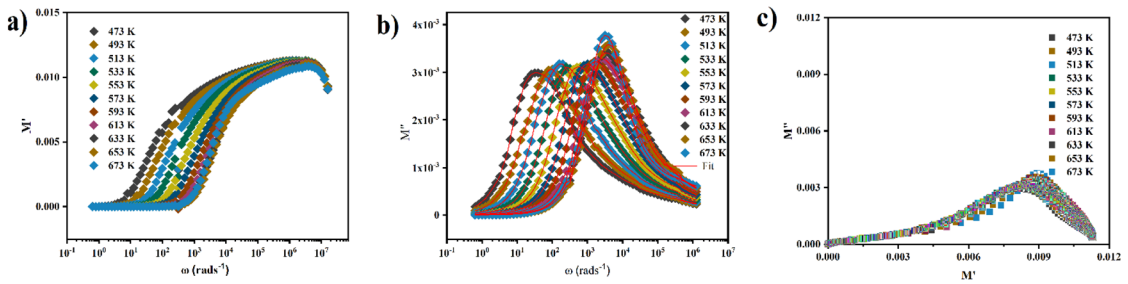

Fig. 8 (a) Variation of M′ with frequency at different temperatures for the entitled compound. (b) Variation of M″ with frequency at different temperatures. (c) Cole–Cole plots of modulus.

Here, M''_{max} denotes the peak magnitude of M'', while ω_{max} corresponds to the frequency at which this maximum occurs.

The complex modulus spectrum (M'' *versus* M') for the $Rb_2Mg_2(WO_4)_3$ compound exhibits distinct semicircular arcs, as illustrated in Fig. 8(c). Two prominent semicircles are evident: the first, at lower frequencies, is attributed to grain (bulk) effects, while the second, appearing at higher frequencies, corresponds to grain boundary contributions. This behavior, consistent with the Nyquist plot shown in Fig. 4, provides strong support for the appropriateness of the selected equivalent circuit model.

Fig. 9(a) and (b) display the frequency dependence of M'' and $-Z''$ at the lowest and highest investigated temperatures, respectively, illustrating the corresponding relaxation behavior of the material. At 473 K, the distinct separation between the M'' and $-Z''$ peak positions suggests localized or short-range charge transport,[33] since the modulus formalism predominantly reflects bulk (grain) dynamics whereas the impedance response is more sensitive to long-range conduction pathways. Conversely, the almost coincident M'' and $-Z''$ peaks at 673 K indicate that both formalisms probe essentially the same relaxation time, which is typically interpreted as evidence of long-range or delocalized charge transport at elevated temperatures.[33]

Charge transport *via* the exponent m

Dielectric permittivity provides essential insight into the intrinsic properties of the investigated material, reflecting its ability to polarize under an applied electric field. The complex dielectric constant is expressed as:[34]

$$\varepsilon^* = \varepsilon' - j\varepsilon'' = \frac{1}{j\omega C_0 Z^*} \quad (9)$$

where ε' denotes the real part, corresponding to stored energy, and ε'' represents the imaginary part, associated with energy dissipation within the material. Here, C_0 is the vacuum capacitance, and $\omega = 2\pi f$ is the angular frequency.

Fig. 10(a) presents the real part of the permittivity, ε', as a function of frequency at various temperatures for the $Rb_2Mg_2(WO_4)_3$ compound. At low frequencies, ε' attains large values, highlighting a strong energy-storage capability in this range, whereas ε' declines with increasing frequency, indicating a reduction in stored energy. At any given frequency, ε' grows with temperature, which is attributed to thermally activated charge carriers that enhance polarization. This response arises from the combined action of ionic, electronic, orientational, and interfacial polarizations, with orientational and interfacial mechanisms dominating the relaxation of polarizability, while ionic and electronic polarizations are mainly associated with resonance effects. Fig. 10(b) presents the frequency dependence of the imaginary permittivity, ε'', measured across multiple temperatures. ε'' is very large at low frequencies (up to about 7.3×10^5) and decreases steadily with frequency before reaching a plateau at the high-frequency end, evidencing strong dielectric dispersion. The systematic shift with temperature indicates thermally activated relaxation, consistent with the causal dielectric response described by complex permittivity. This behavior reflects the combined action of polarization mechanisms: interfacial/space charge and dipolar contributions dominate at low to mid frequencies, while faster ionic and electronic polarizations govern the high-frequency regime.

The literature survey reveals that the temperature dependence of the parameter "m" provides insight not only into the prevailing conduction mechanism but also into the type of charge carriers involved. The insert of Fig. 10(b) presents the double-logarithmic plots of ε'' *versus* frequency at different temperatures for the investigated sample. The evolution of ε'' with frequency and temperature is interpreted within the framework of the model proposed by Giuntini and al[35]

$$\varepsilon'' = (\varepsilon_0 - \varepsilon_\infty)^2 2\pi^2 N \left(\frac{ne}{\varepsilon_0}\right)^3 K_B T \tau_0^m W_M^{-4} \omega^{m(T)} = B\omega^{m(T)} \quad (10)$$

Here, ε_0 denotes the static dielectric constant, ε_∞ is the dielectric constant in the high-frequency limit, n is the number of hopping electrons, e is the elementary charge, N is the density of localized states, T is the absolute temperature, k is the Boltzmann constant, τ_0 is the characteristic relaxation time, and m is the exponent of the angular frequency. The temperature-

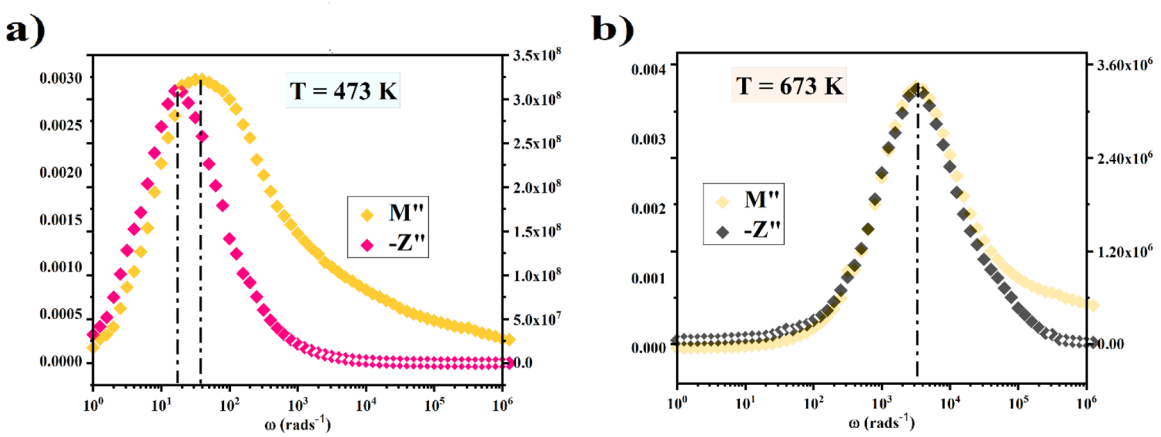

Fig. 9 $-Z''$ & M'' variation with frequency at the lowest (a) and the highest temperature (b).

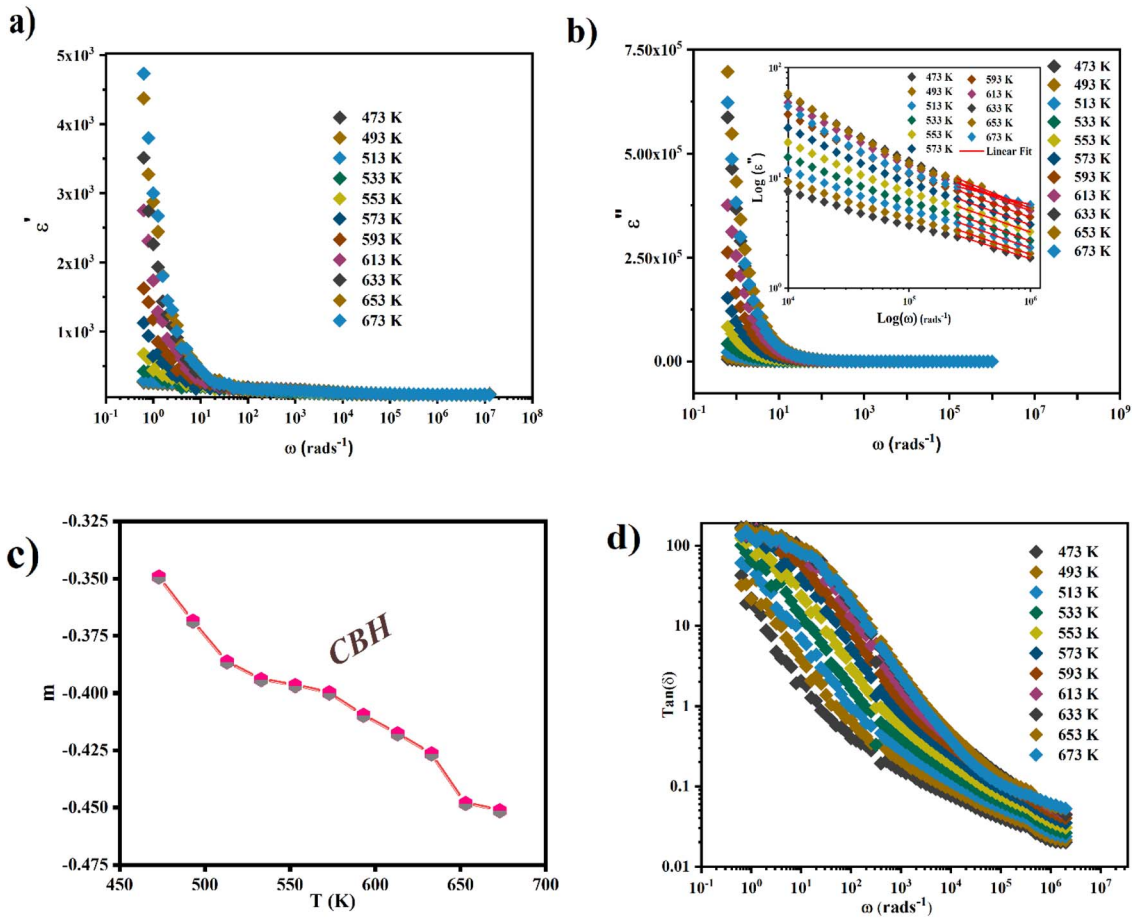

Fig. 10 (a) Frequency-dependent real part (ε') of the dielectric permittivity at different temperatures of $Rb_2Mg_2(WO_4)_3$ compound. (b) Frequency-dependent imaginary part (ε'') of the dielectric permittivity at different temperatures. Insert (b) log(ε'') *vs.* log(ω) of $Rb_2Mg_2(WO_4)_3$ compound. (c) Temperature dependence of the frequency exponent m of $Rb_2Mg_2(WO_4)_3$ compound. (d) Frequency dependence of tan(δ) at different temperatures of $Rb_2Mg_2(WO_4)_3$ compound.

dependent exponent $m(T)$ is obtained from the negative slopes of plots of $\ln(\varepsilon'')$ *versus* $\ln(\omega)$ at different temperatures. The evolution of m with temperature is then used to elucidate the underlying conduction mechanism. As shown in Fig. 10(c), $m(T)$ decreases monotonically with temperature, which strongly supports a CBH conduction process.

The dielectric loss factor, or loss tangent, is defined as the ratio of the imaginary to the real components of permittivity:[36]

$$\mathrm{Tan}\delta = \frac{\varepsilon'}{\varepsilon''} \tag{11}$$

For optoelectronic materials, the dissipation factor tan(δ), plotted in Fig. 10(d), is a key parameter. Here, δ denotes the loss angle between the applied voltage and the charging current. Dielectric losses originate from several processes, such as charge conduction, dielectric relaxation, molecular dipole interactions, and interfacial polarization. At low frequencies, more energy is required to move charge carriers, which leads to higher tan(δ) values. As the frequency rises, the effective resistivity decreases, enabling easier charge transport and consequently lowering the dielectric loss. This frequency-driven decrease in loss underscores the material's promise for integration in electrical and optoelectronic devices. However, when high temperatures are combined with low frequencies, dielectric loss increases markedly, consistent with enhanced electrical conductivity in the material.

Electrical conduction mechanism *via* the conductivity

Fig. 11(a) presents the frequency dependence of the AC conductivity over the temperature interval 473–673 K. In the low-frequency region, the conductivity attains a plateau corresponding to the DC component, which is essentially frequency-independent. At higher frequencies, the conductivity exhibits a marked dispersion arising from the AC contribution. In this regime, charge carriers undergo thermally activated hopping, resulting in random diffusion at low frequencies that yields the DC conductivity σ_{dc}. Meanwhile, in the dispersive region, ions oscillate back and forth in a correlated fashion. According to the jump-relaxation framework developed by Funke and Hoppe,[37] the coexistence of a frequency-independent DC plateau and a frequency-dependent AC part is explained by the balance between successful and unsuccessful hops: at low frequencies,

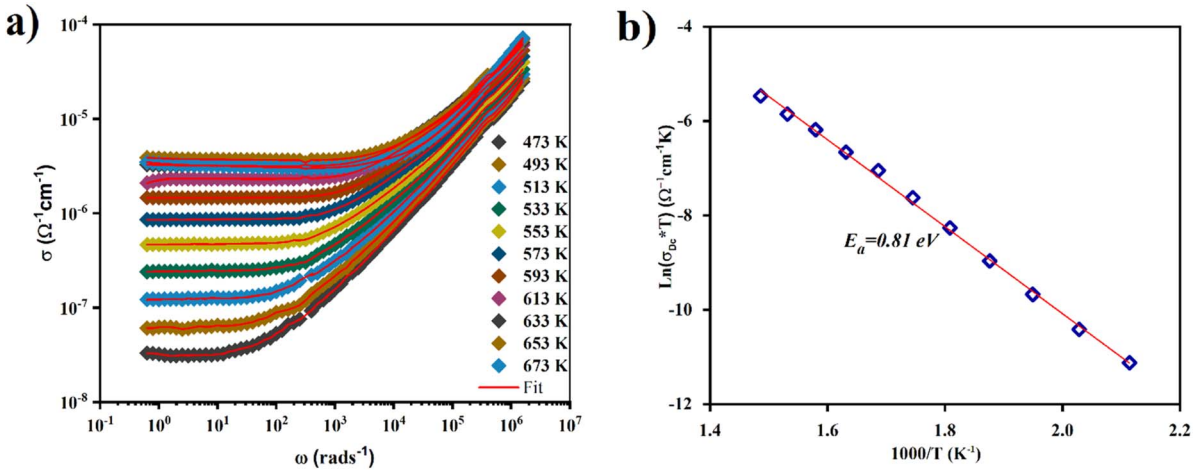

Fig. 11 (a) Variation of σ_{AC} conductivity with temperature at different frequencies, (b) Arrhenius fits of σ_{dc}.

successful long-range hops dominate the transport, whereas at high frequencies the proportion of unsuccessful hops increases, leading to the pronounced dispersion observed in the conductivity spectra.

The AC conductivity spectrum is described by the empirical Jonscher power law:[38]

$$\sigma_{AC} = \sigma_{dc} + A\omega^{s} \quad (12)$$

Here, σ_{dc} denotes the material's DC conductivity, A is the pre-exponential factor, ω is the angular frequency, and s is the power-law exponent. The exponent s characterizes the interaction of mobile ions with the surrounding lattice and usually lies between 0 and 1, a range consistent with several transport mechanisms such as quantum-mechanical tunneling (QMT),[39] non-overlapping small-polaron tunneling (NSPT),[40] correlated barrier hopping (CBH),[40] and overlapping large-polaron tunneling (OLPT).[41] The DC conductivity σ_{dc}, obtained by fitting the Jonscher law over the entire temperature interval, follows an Arrhenius-type behavior; the resulting σ_{dc} *versus* inverse temperature plot derived from complex-impedance analysis is displayed in Fig. 11(b) and obeys Arrhenius' relation:[42]

$$\sigma_{dc} = \sigma_0 \exp\left(\frac{-E_a}{K_B T}\right) \quad (13)$$

From this plot, the activation energy is determined to be 0.82 eV. This value lies within the same interval as those reported for related compounds[7,13] and falls in the range typically associated with semiconducting materials.[43,44]

Fig. 12(a) presents the temperature-dependent evolution of the fitted parameters s and $(1-s)$, highlighting their concurrent variation across the investigated thermal range. The figure reveals a clear decrease in s as temperature rises. When these $s(T)$ results are compared with the theoretical models discussed earlier, they strongly suggest that the correlated barrier hopping (CBH) model is the dominant conduction mechanism. To clarify the conduction mechanism, the AC conductivity of the sample was examined in detail. The resulting frequency-dependent AC conductivity curves for the investigated compound at different temperatures are presented in Fig. 12(b). Within the framework of the CBH model, charge transport proceeds through single-polaron or bipolaron hopping across the coulombic barrier separating localized defect sites. Based on this approach, the corresponding binding energy is evaluated using the following expression:

$$S = \frac{d(\ln(\sigma_{ac}))}{d(\ln \omega)} = 1 - \frac{6kT}{W_M - kT\ln(\omega\tau_0)} \quad (14)$$

Here, τ_0 denotes the characteristic relaxation time, typically comparable to the atomic vibration period. This expression

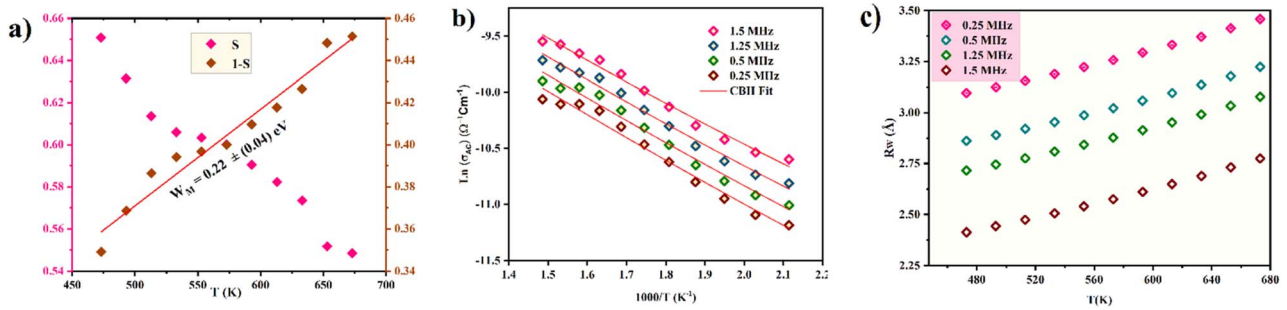

Fig. 12 (a) Evolution of s and 1 s as a function of temperature, (b) ln ($\sigma_{dc}T$) as a function of (1000/T) at different frequencies, (c)Temperature dependence of *Rw* at different frequencies.

Table 2 Obtained parameters of CBH fit

	Frequency (MHz)	U_{eff} (eV)	ε'	N(E_F) (eV^{-1} cm^{-1})	W_m (eV)	σ_{dc} (Ω^{-1} cm^{-1}) (á 658 K)
$Rb_2Mg_2(WO_4)_3$	0.25	0.55	100	2.1 10^{17}	0.21	8.43 10^{-5}
	0.5	0.49		7.8 10^{17}		
	1.25	0.45		8.8 10^{18}		
	1.5	0.39		1.2 10^{19}		

indicates that s depends on both frequency and temperature. For small values of W_m/k_BT, s increases with frequency; however, when W_m/k_BT becomes large, s approaches unity, and its variation with frequency becomes negligible. Under these conditions, eqn (13) simplifies to eqn (14).

$$S = 1 - \frac{6kT}{W_M} \quad (15)$$

According to the CBH model, the AC conductivity can be approximated, to first order, by the relation:[45]

$$\sigma_{ac} = n\frac{\pi^2}{24}NN_P\varepsilon\varepsilon_0\omega R_\omega{}^6 \quad (16)$$

where ε and ε_0 denote the dielectric constants of the material and of free space, respectively; N is the density of paired localized sites; $R\omega$ is the hopping distance; and n represents the number of electrons involved in the hopping event. The product N(E_F) and U_{eff} were determined by fitting the theoretical curves of ln(σ_{AC}) *versus* 1000/T to the experimental data (Fig. 12(b)), and the resulting parameters are summarized in Table 2. As shown, increasing the frequency leads to a reduction in U_{eff}, which is consistent with thermally assisted hopping conduction in this frequency temperature range. Moreover, the density of localized states N increases with frequency, in agreement with the observed rise in AC conductivity.

Fig. 12(c) shows how the hopping distance ($R\omega$) varies with temperature and frequency. Increasing the frequency leads to a reduction in $R\omega$, confirming an inverse dependence between these parameters. Conversely, $R\omega$ becomes larger as the temperature rises, owing to the additional thermal energy that promotes carrier hopping. At low temperatures, $R\omega$ exhibits little variation and remains almost unchanged. Importantly, the extracted hopping distances fall within the scale of the interatomic separation.

Conclusion

$Rb_2Mg_2(WO_4)_3$ emerges as a standout triple tungstate, masterfully engineered *via* solid-state synthesis into a pure cubic phase with uniform microstructure—unlocking unprecedented dielectric prowess for optoelectronics and energy storage. Its Nyquist plots reveal captivating non-Debye relaxation, with dual semicircles spotlighting grain–grain boundary synergy and a temperature-driven surge in charge mobility *via* thermally activated hopping, precisely mapped by the Correlated Barrier Hopping (CBH) model. This synergy yields ultra-low dielectric losses paired with sky-high permittivity, outshining conventional materials and enabling breakthroughs in high-efficiency capacitors and microwave devices. By decoding hopping-dominated conduction and interfacial polarization, this work bridges atomic-scale insights with real-world innovation, propelling $Rb_2Mg_2(WO_4)_3$ toward revolutionizing next-generation microelectronics.

Author contributions

Ines Mbarek: writing – original draft, visualization, methodology, investigation, formal analysis. Saber Nasri: writing – original draft, visualization, methodology, investigation, formal analysis. Iheb Garoyui: writing – review & editing, software, methodology, investigation. Mehdi Akermi: writing – original draft, visualization, methodology, investigation, formal analysis. Writing – original draft, supervision, methodology. Mohamed Tliha: writing – original draft, supervision, validation, project administration. Abderrazek Oueslati: writing – original draft, supervision, validation, project administration.

Conflicts of interest

The authors declare that they have no known competing financial interests or personal relationships that could have appeared to influence the work reported in this paper.

Data availability

Data will be available by request.

Acknowledgements

The authors extend their appreciation to Umm Al-Qura University, Saudi Arabia for funding this research work through grant number: 26UQU4331138GSSR01. Funding statement: this research work was funded by Umm Al-Qura University, Saudi Arabia under grant number: 26UQU4331138GSSR01.

References

1 C. Gu, *et al.*, Tungsten-based nanomaterials in the biomedical field: A bibliometric analysis of research progress and prospects, *Adv. Mater.*, 2023, **35**(1), 2204397.
2 H. L. Abubakar, *et al.*, A review on the applications of zinc tungstate (ZnWO4) photocatalyst for wastewater treatment, *Heliyon*, 2022, **8**(7), 9964.

3 Z. F. Huang, *et al.*, Tungsten oxides for photocatalysis, electrochemistry, and phototherapy, *Adv. Mater.*, 2015, **27**(36), 5309–5327.
4 Y. Yu, *et al.*, Crystal growth, structure, optical properties and laser performance of new tungstate Yb: Na2La4 (WO4) 7 crystals, *Opt. Mater.*, 2021, **111**, 110653.
5 P. Sharma, *et al.*, Effect of the anionic counterpart: Molybdate vs. tungstate in energy storage for pseudo-capacitor applications, *Nanomaterials*, 2021, **11**(3), 580.
6 R. Packiaraj, *et al.*, Investigation on the structural, morphological and electrochemical properties of nickel tungstate for energy storage application, *Inorg. Chem. Commun.*, 2021, **126**, 108490.
7 I. Mbarek, *et al.*, Study on structural, morphological, optical and dielectric properties of Na4Mg (WO4) 3 triple tungstate, *J. Mater. Sci.: Mater. Electron.*, 2025, **36**(32), 2047.
8 W. Ge, *et al.*, The thermal and optical properties of BaWO4 single crystal, *J. Cryst. Growth*, 2005, **276**(1–2), 208–214.
9 M. Dayanithy, *et al.*, Synergistic integration of $NiCo_2O_4$ and $NiWO_4$ nanosheets on Ni foam for advanced supercapacitor applications, *J. Porous Mater.*, 2025, **32**(6), 2127–2137.
10 V. Q. Trung, *et al.*, Enhancing photocatalytic performance in Bi2WO6 nanolayers via ultrasound-assisted oxygen vacancy engineering, *J. Alloys Compd.*, 2025, **10**(10), 177747.
11 V. Shevchuk and I. Kayun, Dipole relaxation, dielectric and electric properties of PbWO4 crystals, *Funct. Mater.*, 2005, 297.
12 S. Obbade, *et al.*, Synthesis and crystal structure of new uranyl tungstates M2 (UO2)(W2O8)(M= Na, K), M2 (UO2) 2 (WO5) O (M= K, Rb), and Na10 (UO2) 8 (W5O20) O8, *J. Solid State Chem.*, 2003, **172**(2), 305–318.
13 M. Akermi, *et al.*, Investigating Li 2 Mg 2 (WO 4) 3: structure, morphology, and electrical properties with ultra-low dielectric loss for optimizing laser host materials, *RSC Adv.*, 2025, **15**(17), 13064–13075.
14 S. Han, *et al.*, Effect of the cation size on the framework structures of magnesium tungstate, A 4 Mg (WO 4) 3 (A= Na, K), R 2 Mg 2 (WO 4) 3 (R= Rb, Cs), *Dalton Trans.*, 2015, **44**(12), 5810–5817.
15 H. M. Rietveld, The rietveld method, *Phys. Scr.*, 2014, **89**(9), 098002.
16 P. Jangade, P. Arjunwadkar and M. Nagarbawadi, Structural characterization of lead titanate (PbTiO3) sample using FULLPROF, *IOSR J. Appl. Phys.*, 2016, **8**(6), 52–60.
17 U. Holzwarth and N. Gibson, The Scherrer equation versus the'Debye-Scherrer equation', *Nat. Nanotechnol.*, 2011, **6**(9), 534.
18 A. B. Schroeder, *et al.*, The ImageJ ecosystem: Open-source software for image visualization, processing, and analysis, *Protein Sci.*, 2021, **30**(1), 234–249.
19 A. Ortega and F. Nieto, Quantitative EDX analysis in TEM, *Practical development, limitations and standards, Science, Technology and Education of Microscopy: an Overview*, 2003, pp. 687–694.
20 E. K. Gibson Jr, Volatile elements, carbon, nitrogen, sulfur, sodium, potassium and rubidium in the lunar regolith, *Phys. Chem. Earth*, 1977, **10**, 57–62.
21 E. A. Pringle and F. Moynier, Rubidium isotopic composition of the Earth, meteorites, and the Moon: Evidence for the origin of volatile loss during planetary accretion, *Earth Planet. Sci. Lett.*, 2017, **473**, 62–70.
22 T. Charpin, *et al.*, Study of the volatilization of cesium and rhenium in the waste vitrification process, *J. Nucl. Mater.*, 2022, **558**, 153381.
23 R. Hill and L. Dissado, Debye and non-Debye relaxation, *J. Phys. C: Solid State Phys.*, 1985, **18**(19), 3829.
24 P. Córdoba-Torres, T. J. Mesquita and R. P. Nogueira, Relationship between the origin of constant-phase element behavior in electrochemical impedance spectroscopy and electrode surface structure, *J. Phys. Chem. C*, 2015, **119**(8), 4136–4147.
25 M. Schwarze, *et al.*, Molecular parameters responsible for thermally activated transport in doped organic semiconductors, *Nat. Mater.*, 2019, **18**(3), 242–248.
26 B.-A. Mei, *et al.*, Physical interpretations of Nyquist plots for EDLC electrodes and devices, *J. Phys. Chem. C*, 2018, **122**(1), 194–206.
27 Z. Kukuła, *et al.*, Electric relaxation of superparamagnetic Gd-doped lead molybdato-tungstates, *Ceram. Int.*, 2019, **45**(4), 4437–4447.
28 P. Macedo, M. CT, and R. Bose, *The Role of Ionic Diffusion in Polarisation in Vitreous Ionic Conductors*. 1972.
29 D. Speer and E. Salje, Phase transitions in langbeinites I: Crystal chemistry and structures of K-double sulfates of the langbeinite type M 2++ K2 (SO4) 3, M++= Mg, Ni, Co, Zn, Ca, *Phys. Chem. Miner.*, 1986, **13**(1), 17–24.
30 Z. Yang, *et al.*, Phase equilibria and crystal chemistry of the R–Cu–Ti–O systems (R= lanthanides and Y), *J. Solid State Chem.*, 2009, **182**(5), 1142–1148.
31 W. Zhu, *et al.*, Mechanism of Th4+, Zr4+ doping in PbWO4 crystals, *Solid State Commun.*, 2003, **125**(5), 253–257.
32 R. Bergman, General susceptibility functions for relaxations in disordered systems, *J. Appl. Phys.*, 2000, **88**(3), 1356–1365.
33 J. Chen, *et al.*, Localized electrons enhanced ion transport for ultrafast electrochemical energy storage, *Adv. Mater.*, 2020, **32**(14), 1905578.
34 R. Sengupta, *et al.*, Measurement of complex dielectric constant using optical method, *IEEE Trans. Instrum. Meas.*, 2018, **68**(6), 1814–1820.
35 L. Giuntini, *et al.*, Coupled CFD and 1-D dynamic modeling for the analysis of industrial Regenerative Thermal Oxidizers, *Chem. Eng. Process. Process Intensif.*, 2020, **157**, 108117.
36 M. Sebastian, R. Ubic and H. Jantunen, Low-loss dielectric ceramic materials and their properties, *Int. Mater. Rev.*, 2015, **60**(7), 392–412.
37 K. Funke and R. Hoppe, Jump-relaxation model yields Kohlrausch-Williams-Watts behaviour, *Solid State Ionics*, 1990, **40**, 200–204.

38 A. Lukichev, Nonlinear relaxation functions. Physical meaning of the Jonscher's power law, *J. Non-Cryst. Solids*, 2016, **442**, 17–21.
39 P. R. Schreiner, Quantum mechanical tunneling is essential to understanding chemical reactivity, *Trends Chem.*, 2020, **2**(11), 980–989.
40 A. Zaafouri and M. Megdiche, Experimental and theoretical study of AC electrical conduction mechanisms by NSPT model of LiNa3-xAgxP2O7 (x= 0.2 and 0.6) ceramic compounds, *Ionics*, 2017, **23**(5), 1155–1164.
41 S. Kumar, A. Shukla and K. Sreenivas, Overlapping large polaron tunnelling (OLPT) type conduction mechanism in magnesium ferrite (MgFe2O4) ceramics, *Appl. Phys. A*, 2022, **128**(5), 381.
42 M. Lewerenz, *et al.*, New method evaluating currents keeping the voltage constant for fast and highly resolved measurement of Arrhenius relation and capacity fade, *J. Power Sources*, 2017, **353**, 144–151.
43 O. d. Macedo, A. d. Oliveira and I. d. Santos, Zinc tungstate: a review on its application as heterogeneous photocatalyst, *Ceramica*, 2022, **68**(387), 294–315.
44 D. Meziani, *et al.*, Physicochemical characterizations and semiconducting properties of a manganese tungstate MnWO4 obtained by hydrothermal route, *J. Solid State Electrochem.*, 2021, **25**(7), 2097–2106.
45 P. K. Singh, *et al.*, Study of dielectric relaxation and thermally activated ac conduction in multicomponent Ge10−xSe60Te30Inx (0≤ x≤ 6) chalcogenide glasses using CBH model, *Results Phys.*, 2019, **12**, 223–236.